applied sciences

MDPI

Article

Output Filter Design for a Novel Dual-Input PV-Wind Power Converter by Energy Balance Principle

Chih-Lung Shen * and You-Sheng Shen

Department of Electronic Engineering, National Kaohsiung First University of Science and Technology, Yanchao District, Kaohsiung 82445, Taiwan; u0415903@nkfust.edu.tw

* Correspondence: clshen@ccms.nkfust.edu.tw; Tel.: +886-925-871-685

Academic Editor: Teen-Hang Meen

Received: 24 July 2016; Accepted: 9 September 2016; Published: 16 September 2016

Abstract: In this paper, a detailed and systematic derivation of the output filter in a novel dual-input photovoltaic (PV)-wind converter (DIPWC) is presented. The theoretical derivation is based on an energy balance principle. While the DIPWC operates in steady state, the amount of charged energy of the output filter will be equal to that of the energy pumped away within one switching cycle. From this zero net change in energy, the minimum value of the output filter can be found. With the determined value, the DIPWC is able to operate in continuous conduction for high power applications. The developed procedure of the inductance determination can be applied to other types of dual-input converters. Therefore, it makes significant contributions to the design toward a green-energy, multi-input converter. To verify the correctness of the mathematical analysis, the DIPWC—with the derived output inductance—is built and tested. Practical measurements and results have verified the inductance determination.

Keywords: PV-wind power converter; green energy; multi-input converter; energy balance principle; inductance derivation

1. Introduction

Nowadays, renewable energies, such as photovoltaic (PV), wind energy and hydroelectric, have been widely adopted as alternatives to fossil fuels. However, output power of a renewable-energy generator is highly affected by atmospheric conditions. Therefore, a hybrid power system—including two or more input sources—has become the design trend for renewable energy processing, in which a constant output voltage and sustained power supply can be completed [1–6].

A dual-input converter (DIC) can simultaneously deal with two inputs and obtains a regulated voltage [7–12]. For renewable power applications, a DIC should have the ability to process renewable energy for each individual input. Even though neither of the inputs has the power to feed, the DIC can still function well. In addition, the DC-bus voltage of a grid-connected system is normally up to 380 V. That is, the DIC must be capable of achieving a high step-up feature [13–21]. In order to meet the marketable requirements, a DIC should have the features of high efficiency, cost-effectiveness, a low electromagnetic interference (EMI), small size, minimum component counts, and a low current ripple. In [22,23], an isolated DIC with multi-windings, based on the flux additivity concept, is proposed to accomplish some of the mentioned features. However, each power MOSFET in the DIC has to be in series with a reverse-blocking diode, which results in the energy stored in the leakage inductors not being recycled and causes a high voltage spike on MOSFET during turn-on and turn-off transitions. Adopting a clamp circuit or snubber may be an approach to alleviate the mentioned voltage spike and to reduce power loss [24]. Nevertheless, this approach increases the power component count and cannot improve the voltage conversion ratio.

In this paper, a novel power DIC is presented, which can process PV power and wind-turbine energy simultaneously or individually and its so called novel dual-input PV-wind converter (DIPWC). For continuous current operation and output voltage regulation, the output port adopts a second-order LC filter in cascade connection to the converter. The inductance of the output filter will dominate the feature of the DIPWC. However, the determination of the inductance has a sophisticated procedure. Therefore, this paper will first describe the operation of the DIPWC and then design the inductance theoretically.

Following the introduction in Section 1, the remainder of this paper is organized as follows. Section 2 briefly introduces the characteristics of the proposed DIPWC. The circuit operation principle of the converter and control mechanism are discussed in Section 3. A theoretical analysis for determining an optimal value of the output inductor is presented in Section 4. To verify the correctness of the theoretical analysis, a DIPWC prototype with the designed filter is built. Key experimental results will be illustrated in Section 5. Finally, Section 6 summarizes the conclusions.

2. Characteristics of Proposed Converter

Figure 1 shows the circuit configuration of the proposed DIPWC in this paper, which mainly consists of two coupled inductors, four power MOSFETs, four capacitors, ten diodes, and an LC filter. The proposed DIPWC can conceptually be regarded as the integrating of two double-ended forwards with voltage multipliers. This structure can recycle the energy stored in the leakage inductors, $L_{k,wind}$ and $L_{k,pv}$, to their corresponding power inputs. By controlling the appropriate power switches with pulse-width modulation (PWM), the DIPWC can draw renewable energy and then feed power to the DC bus. The input renewable energy can come from either a PV panel, a wind turbine or both. During a switch cycle, when all the switches are in an off state, the output inductor L_o has to release energy to the DC bus to continually provide power. A renewable generation system—to deal with the high power rating—will accompany a high level of output current. As a result, the DIPWC should operate in continuous conduction mode (CCM) to lower current stresses of semiconductor devices. This reason has revealed the importance of the design relating to output-filter inductance.

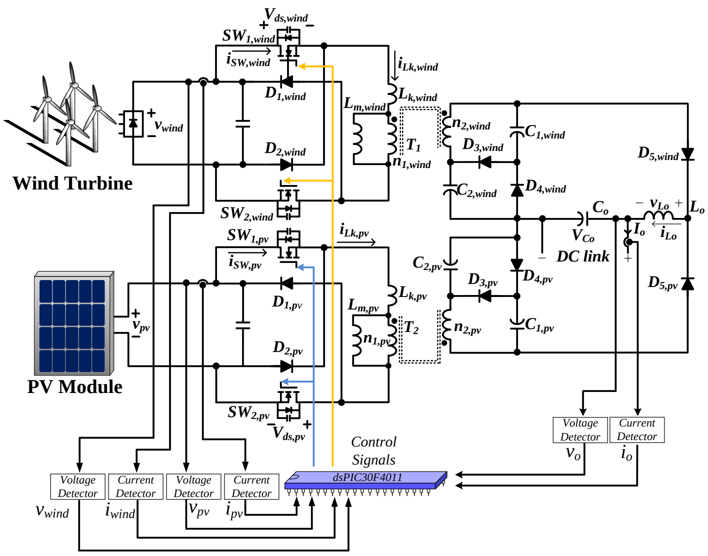

Figure 1. The configuration of the presented dual-input photovoltaic-wind converter (DIPWC).

3. Operation Principle

The operation of the DIPWC can be divided into six stages. Figure 2 shows the related equivalents, while corresponding key waveforms are depicted in Figure 3. In Figure 1, the magnetizing inductances,

$L_{m,wind}$ and $L_{m,pv}$, are both in CCM. To simplify the circuit analysis, there are some assumptions made in the following.

(1) In Figure 2, capacitances of $C_{1,wind}$, $C_{2,wind}$, $C_{1,pv}$, and $C_{2,pv}$ are large enough so that all the voltages across them can be regarded as constant in a switching cycle.
(2) The internal resistances and parasitic capacitances in all active switches are neglected.
(3) All diodes are ideal.

Stage 1 [t_0, t_1]: Refer to Figure 2a for Stage 1. Switches $SW_{1,wind}$ and $SW_{2,wind}$ are closed, whereas $SW_{1,pv}$ and $SW_{1,pv}$ are opened. The wind-turbine input voltage V_{wind} forward energy to $L_{m,wind}$ via the loop of V_{wind}-$SW_{1,wind}$-$L_{k,wind}$-$L_{m,wind}$-$SW_{2,wind}$. Meanwhile, the output inductor L_o and capacitor C_o absorb energy from $C_{2,wind}$, so that the current flowing through L_o, i_{Lo}, increases linearly. The capacitor $C_{2,pv}$ is charged by the magnetizing inductor $L_{m,pv}$. This stage ends as the $SW_{1,wind}$ and $SW_{2,wind}$ are turned off.

Stage 2 [t_1, t_2]: The equivalent of Stage is shown in Figure 2b. During this time interval, all the switches are open. The leakage inductor $L_{k,wind}$ dumps energy to capacitor C_{wind} via the loop of $L_{k,wind}$-$D_{1,wind}$-C_{wind}-$D_{2,wind}$. The current of the leakage inductor $L_{k,wind}$, $i_{Lk,wind}$, decreases rapidly. At output, the L_o powers output and its current decreases accordingly. This stage ends when the current $i_{Lk,wind}$ falls to 0.

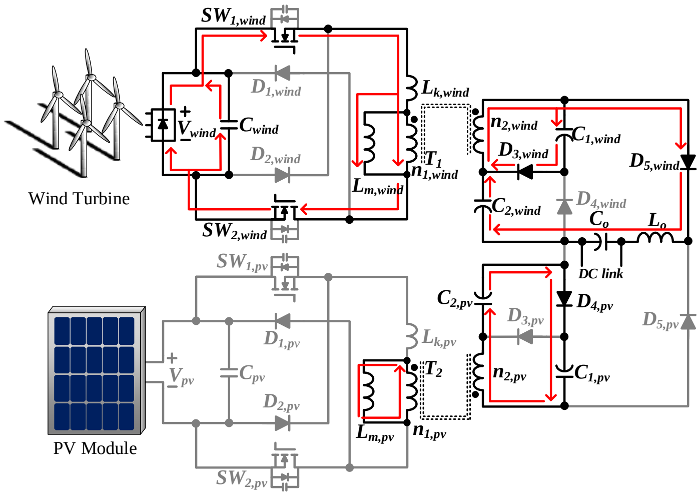

(**a**)

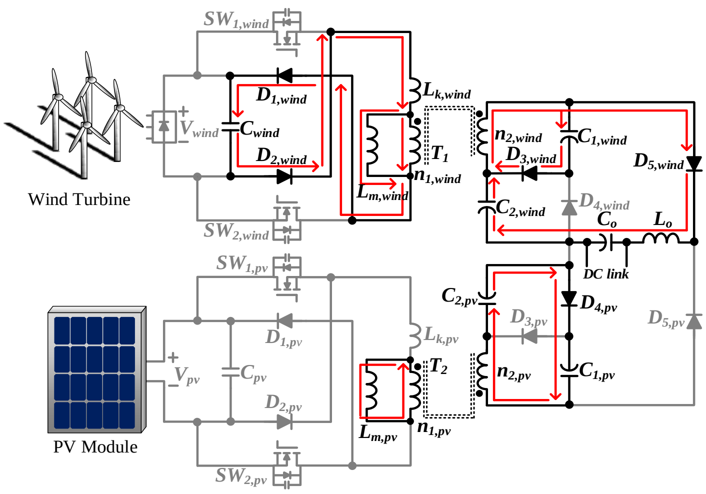

(**b**)

Figure 2. *Cont.*

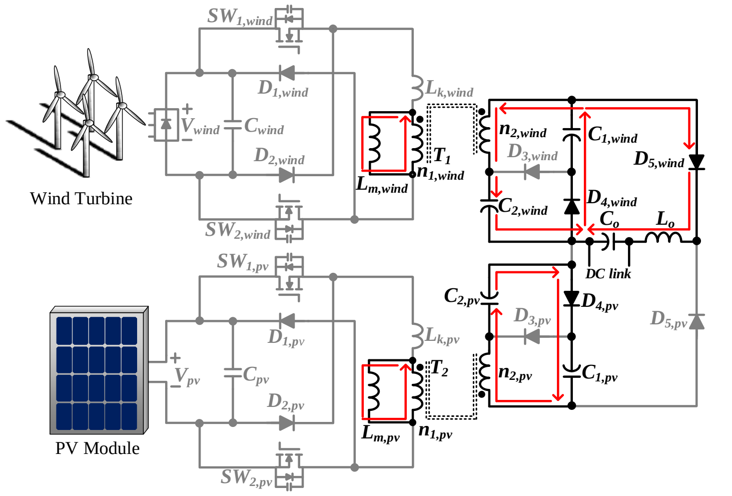

(**c**)

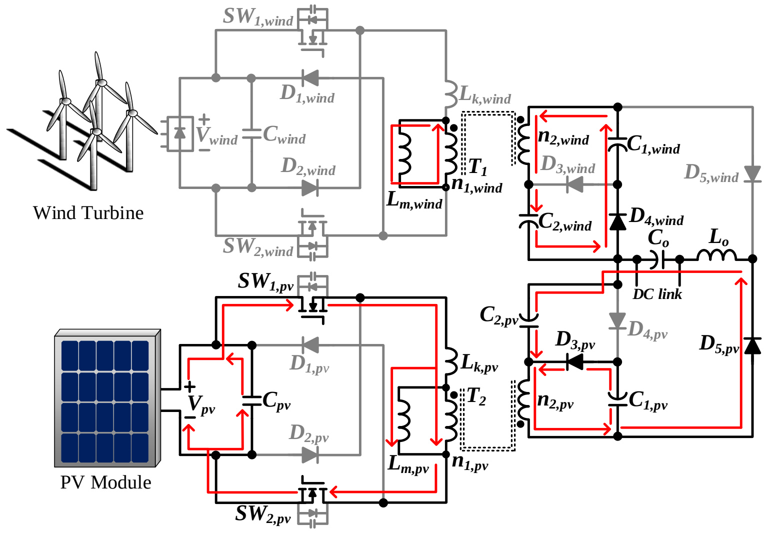

(**d**)

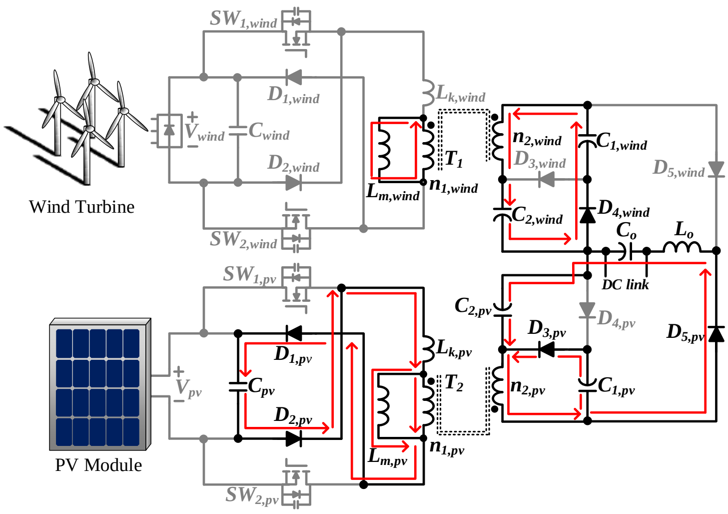

(**e**)

Figure 2. *Cont.*

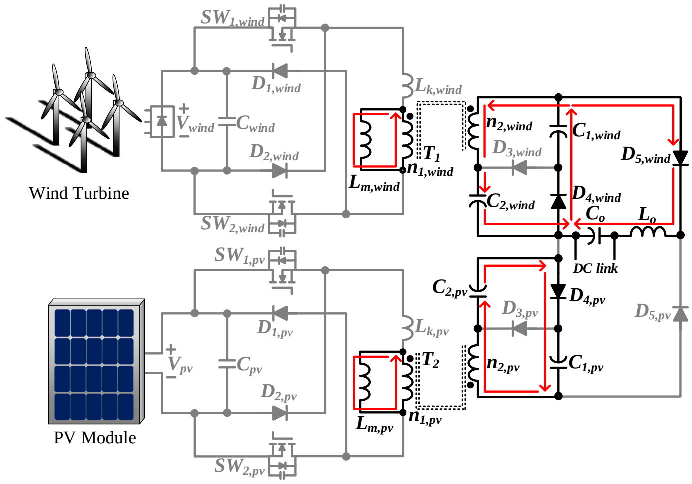

(**f**)

Figure 2. Equivalent circuits of the DIPWC: (**a**) Stage 1, (**b**) Stage 2, (**c**) Stage 3, (**d**) Stage 4, (**e**) Stage 5, and (**f**) Stage 6.

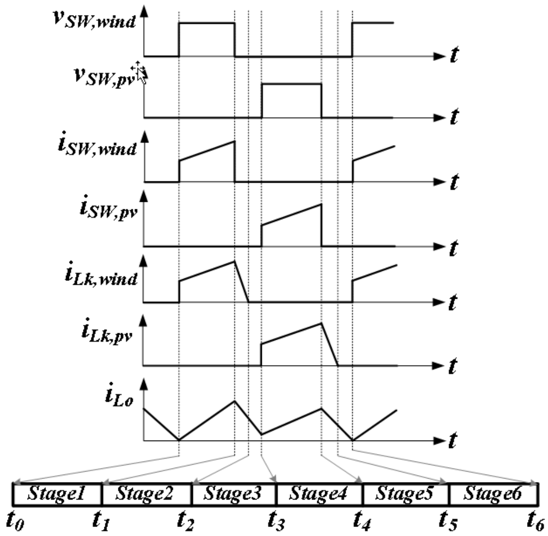

Figure 3. Conceptual key waveforms of the DIPWC.

Stage 3 [t_2, t_3]: Figure 2c depicts the equivalent circuit of this stage, in which all the switches are open. Magnetizing inductors, $L_{m,wind}$ and $L_{m,pv}$, release their energy to $C_{2,wind}$ and $C_{2,PV}$, respectively. The capacitor $C_{1,wind}$ charges C_o by the loop of C_o-$D_{4,wind}$-$C_{1,wind}$-$D_{5,wind}$-L_o. The operation of the converter enters into the next stage when $SW_{1,pv}$ and $SW_{2,pv}$ are simultaneously turned off.

Stage 4 [t_3, t_4]: This stage begins at $t = t_4$. Figure 2d illustrates the equivalent. In Stage 4, both switches $SW_{1,pv}$ and $SW_{2,pv}$ are closed, whereas $SW_{1,wind}$ and $SW_{1,wind}$ are opened. The PV input voltage V_{pv} forwards energy to $L_{m,pv}$ through the loop of V_{pv}-$SW_{1,pv}$-$L_{k,pv}$-$L_{m,pv}$-$SW_{2,pv}$. The energy stored in the magnetizing inductor $L_{m,wind}$ is released to the secondary of the coupled inductor T_1 to charge $C_{2,wind}$. The inductor L_o and capacitor C_o absorb energy from $C_{2,pv}$; therefore, the current of L_o, i_{Lo}, increases linearly. As the $SW_{1,pv}$ and $SW_{2,pv}$ are turned off again, this stage ends.

Stage 5 [t_4, t_5]: As referred to in Figure 2e, it can be found that all the switches are in an off state in Stage 5. The leakage inductor $L_{k,pv}$ charges capacitor C_{pv} and its current drops steeply. In addition, output inductor L_o pumps energy to C_o, which results in a linear decrease at current i_{Lo}. At the moment that current $i_{Lk,pv}$ drops to 0, Stage 6 begins.

Stage 6 [t_5, t_6]: Figure 2f shows the equivalent circuit of this stage, in which all the switches are open. Capacitors $C_{2,wind}$ and $C_{2,pv}$ are charged by magnetizing inductors, $L_{m,wind}$ and $L_{m,pv}$, respectively. The output absorbs energy from $C_{1,wind}$ via the loop of C_o-$D_{4,wind}$-$C_{1,wind}$-$D_{5,wind}$-L_o. When $SW_{1,wind}$ and $SW_{2,wind}$ are turned on again, this stage ends and the operation of the DIPWC over one switch cycle is completed.

To achieve MPPT, the simplest MPPT algorithm, the perturb-and-observe method, is adopted to reach the maximum power point, as shown in Figure 4. The MPPTs for the wind turbine and PV module are controlled independently. Accordingly, the terminal voltages and currents of the wind turbine and PV module, v_{wind}, i_{wind}, v_{pv} and i_{pv}, have to be detected for the calculation of each input power. Then, based on the truth table and the corresponding flowchart, as shown in Table 1 and Figure 5, respectively, duty ratios of the four active switches are determined for MPPT accomplishment. All the control is completed by a microcontroller dsPIC30F4011, which is illustrated in Figure 1.

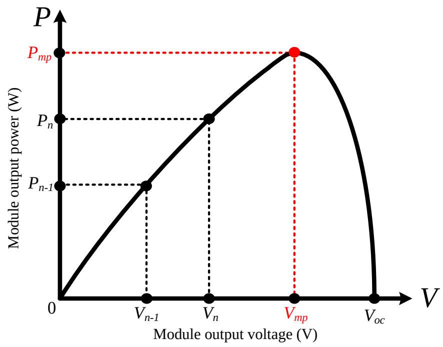

Figure 4. P-V curve of photovoltaic (PV) module.

Table 1. Truth table of the perturb-and-observe method.

P_n > *Pn-1*	V_n > *Vn-1*	Related Position	Duty Cycle (*D*)
True	True	Left	Decrease
True	False	Right	Increase
False	True	Right	Increase
False	False	Left	Decrease

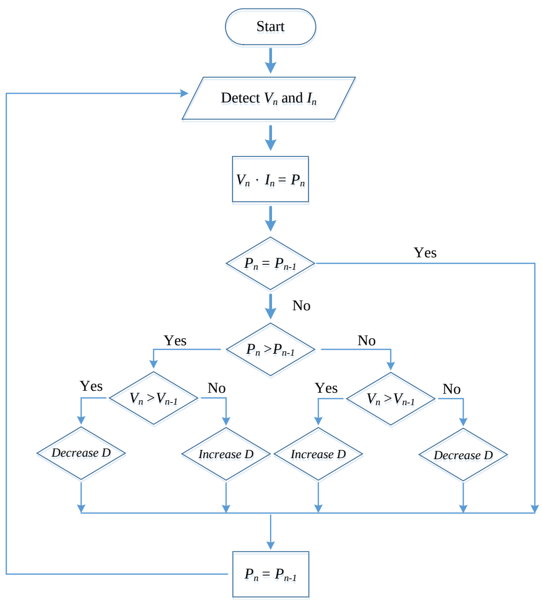

Figure 5. The flowchart of the perturb-and-observe method.

4. Inductance Derivation

Conceptual waveforms of gate signals and output inductor voltage and current are illustrated in Figure 6, in which the switches $SW_{1,wind}$ and $SW_{2,wind}$ are closed for $D_{wind}T_s$ and $SW_{1,pv}$ and $SW_{2,pv}$ are closed for $D_{pv}T_s$, respectively. Since the voltage ripple at each capacitor is much less than the average capacitor voltage, the voltage across the output inductor can be regarded as constant under all switch statuses. Accordingly, the current flowing through the output inductor will be piecewise linear over one switching cycle. The derivation of the output inductance of the DIPWC is sophisticated. For a clear description, the related procedure is summarized as follows.

Step 1: Find the voltages across $C_{1,wind}$ and $C_{1,pv}$, $V_{C1,wind}$ and $V_{C1,pv}$.
Step 2: Apply energy balance principle to $L_{m,wind}$ and $L_{m,pv}$ to determine the voltages across $C_{2,wind}$ and $C_{2,pv}$, respectively.
Step 3: Apply volt-second balance criterion (VSBC) to L_o to determine the output capacitor voltage V_{Co}.
Step 4: After obtaining all capacitor voltages $V_{C1,wind}$, $V_{C2,wind}$, $V_{C1,pv}$, $V_{C2,pv}$, and V_{Co}, calculate the voltage levels of L_o during the intervals of $D_{wind}T_s$, $D_{pv}T_s$, and $(1 - D_{wind} - D_{pv})T_s$.
Step 5: Find the inductor currents at the time points, $t = D_1T_s$, D_2T_s, and D_3T_s, as shown in Figure 6.
Step 6: Estimate the average current of L_o, $I_{Lo,avg}$.
Step 7: From the equation of $I_{Lo,avg}$ obtained in Step 6, find the minimum inductance of L_o for the CCM operation.

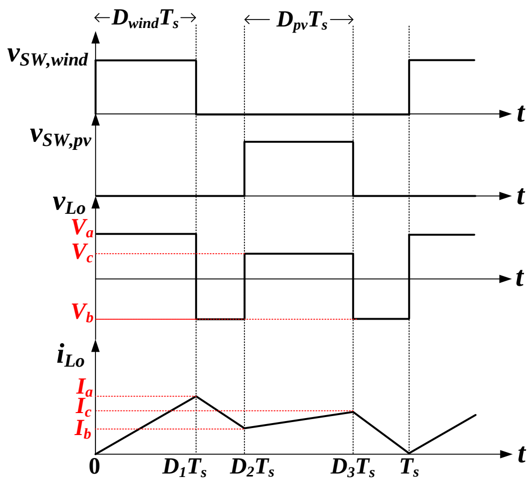

Figure 6. The waveforms for the understanding of inductance derivation.

Following the previous seven steps, a detailed derivation of output inductance is presented below. From Figure 2a, it can be observed that the voltage $V_{C1,wind}$ is n times the magnitude of V_{wind} if the leakage inductor $L_{k,wind}$ is neglected. That is,

$$V_{C1,wind} = n_{wind}V_{wind} \tag{1}$$

Meanwhile, the current increment on magnetizing inductor $L_{m,wind}$ can be estimated by

$$\Delta i_{Lm,wind,+} = \frac{V_{wind}}{L_{m,wind}}D_{wind}T_s \tag{2}$$

When switches $SW_{1,wind}$ and $SW_{2,wind}$ are both turned off, the voltage polarity of $L_{m,wind}$ reverses. The energy stored in $L_{m,wind}$ will be forwarded to the secondary of the coupled inductor T_1 to charge the capacitor $C_{2,wind}$, and then the current $i_{Lm,wind}$ decreases. The descent is calculated as:

$$\Delta i_{Lm,wind,-} = \frac{V_{C2,wind} - V_{C1,wind}}{n_{wind} L_{m,wind}} (1 - D_{wind}) T_s \tag{3}$$

Based on the energy balance principle, that is, net current change in $L_{m,wind}$ being zero, the voltage across $C_{2,wind}$ can be expressed as:

$$V_{C2,wind} = \frac{n_{wind} V_{wind}}{1 - D_{wind}} \tag{4}$$

Similarly, from Figure 2d, in which the switches $SW_{1,pv}$ and $SW_{2,pv}$ are closed, the voltage $V_{C1,pv}$ and the current increment on the magnetizing inductor $L_{m,pv}$ can be represented by:

$$V_{C1,pv} = n_{pv} V_{pv} \tag{5}$$

and

$$\Delta i_{Lm,pv,+} = \frac{V_{pv}}{L_{m,pv}} D_{pv} T_s \tag{6}$$

respectively. Once $SW_{1,pv}$ and $SW_{2,pv}$ are turned off, the capacitor $C_{2,pv}$ begins absorbing energy from $C_{1,pv}$, resulting in current decrease in $L_{m,pv}$. The current drop is estimated as follows:

$$\Delta i_{Lm,pv,-} = \frac{V_{C2,pv} - V_{C1,pv}}{n_{pv} L_{m,pv}} (1 - D_{pv}) T_s \tag{7}$$

In steady state, net current change is zero, which yields:

$$V_{C2,pv} = \frac{n_{pv} V_{pv}}{1 - D_{pv}} \tag{8}$$

Subsequently, the finding for V_{Co} is discussed. When the switches $SW_{1,wind}$ and $SW_{2,wind}$ are in the on state, the output inductor L_o will absorb energy from $C_{2,wind}$ via the loop of C_o-$C_{2,wind}$-$n_{2,wind}$-$D_{5,wind}$-L_o. Thus, the voltage across L_o over the time interval $D_{wind}T_s$ can be given by:

$$V_{Lo,wind} = n_{wind} V_{wind} \frac{2 - D_{wind}}{1 - D_{wind}} - V_{Co} \tag{9}$$

During the interval $D_{pv}T_s$, the switches $SW_{1,pv}$ and $SW_{2,pv}$ are in the on state, which results in the output inductor L_o absorbing energy from $C_{2,pv}$ via the loop of C_o-$C_{2,pv}$-$n_{2,pv}$-$D_{5,pv}$-L_o. In this time interval, the voltage across L_o becomes:

$$V_{Lo,pv} = n_{pv} V_{pv} \frac{2 - D_{pv}}{1 - D_{pv}} - V_{Co} \tag{10}$$

As shown in Figure 2c, the statuses of the four switches are open in the remaining time of a switching period, $(1 - D_{wind} - D_{pv})T_s$. The inductor L_o releases energy and its voltage is valued as:

$$V_{Lo,off} = n_{wind} V_{wind} - V_{Co} \tag{11}$$

By applying VSBC to L_o and deriving with Equations (9)–(11), the following relationship holds:

$$\left[n_{wind} V_{wind} \frac{2 - D_{wind}}{1 - D_{wind}} - V_{Co}\right] D_{wind} + \left[n_{pv} V_{pv} \frac{2 - D_{pv}}{1 - D_{pv}} - V_{Co}\right] D_{pv} + (n_{wind} V_{wind} - V_{Co})(1 - D_{wind} - D_{pv}) = 0 \tag{12}$$

Rearranging equation (12), one can obtain the following representation of V_{Co}:

$$V_{Co} = n_{\text{wind}} V_{wind} [\frac{1 - D_{pv} + D_{pv} D_{wind}}{1 - D_{wind}}] + n_{pv} V_{pv} [\frac{D_{pv}(2 - D_{pv})}{1 - D_{pv}}] \tag{13}$$

The values of V_a, V_b and V_c shown in Figure 6 can be found by substituting (13) into (9), (10), and (11).

$$V_a = n_{wind} V_{wind} (1 + D_{pv}) - n_{pv} V_{pv} \frac{D_{pv}(2 - D_{pv})}{1 - D_{pv}} \tag{14}$$

$$V_b = n_{wind} V_{wind} (\frac{D_{pv} - D_{wind} - D_{pv} D_{wind}}{1 - D_{wind}}) - n_{pv} V_{pv} \frac{D_{pv}(2 - D_{pv})}{1 - D_{pv}} \tag{15}$$

and

$$V_c = n_{pv} V_{pv} (2 - D_{pv}) - n_{wind} V_{wind} (\frac{1 - D_{pv} + D_{pv} D_{wind}}{1 - D_{wind}}) \tag{16}$$

Once V_a, V_b and V_c have been determined, the inductor currents at the time points, $t = D_1T_s$, D_2T_s, and D_3T_s, can be readily calculated. The current magnitudes at these time points are I_a, I_b, and I_c, in turn, which are estimated as follows:

$$I_a = \frac{V_a}{L} D_{wind} T_s \tag{17}$$

$$I_b = I_a + \frac{V_b}{L} (D_2 - D_{wind}) T_s \tag{18}$$

and

$$I_c = I_b + \frac{V_c}{L} D_{pv} T_s \tag{19}$$

In Step 6, the average current of i_{Lo}, $I_{Lo,avg}$, is the integral over the period T_s. That is,

$$\begin{aligned} I_{Lo,avg} &= \tfrac{1}{T_s} (\textstyle\int_0^{D_1 T_s} \tfrac{I_a}{D_1 T_s} x dx + \int_0^{(D_2 - D_1) T_s} \left[\tfrac{I_b - I_a}{(D_2 - D_1) T_s} x + I_a \right] dx + \int_0^{(D_3 - D_2) T_s} \left[\tfrac{I_c - I_b}{(D_3 - D_2) T_s} x + I_b \right] dx \\ &+ \textstyle\int_0^{(1 - D_3) T_s} \left[\tfrac{-I_c}{(1 - D_3) T_s} x + I_c \right] dx) \end{aligned} \tag{20}$$

Calculating and simplifying the equation (20) results:

$$I_{Lo,avg} = \frac{I_a D_2 + I_b (D_2 + D_{pv} - D_{wind}) + I_c (1 - D_2)}{2} \tag{21}$$

According to Ampere Second Balance (ASBC), the average current of the output capacitor C_o should be zero. As a result, the current $I_{Lo,avg}$ is equal to the load current I_o. Then, substituting (14), (15), (16), (17), (18), and (19) into (21), one can obtain the minimum inductance of L_o for CCM as follows:

$$L_o = \frac{(-2 + D_{pv}) D_{pv} (-1 + 2D_2 + D_{pv}) n_{pv} T_s V_{pv} - (-1 + D_{pv})(D_{pv}(-1 + 2D_2 + D_{pv}) + D_{wind}) n_{wind} T_s V_{wind}}{2(1 - D_{pv}) I_o} \tag{22}$$

With respect to capacitor design, voltage ripple dominates capacitance determination. Voltage ripple across a capacitor, Δv_c, can be found by:

$$\Delta v_c = \frac{\Delta Q}{C} = \frac{i_c \Delta t}{C} \tag{23}$$

where Δv_c stands for charge variation during time interval Δt, i_c is the current flowing through the capacitor, and C is the corresponding capacitance. The currents of capacitors $C_{1,wind}$, $C_{2,wind}$, $C_{1,pv}$, $C_{2,pv}$ and C_o are $i_{D3,wind}$, $i_{D4,wind}$, $D_{3,pv}$, $D_{4,pv}$ and i_{Lo}-I_o, respectively. According to the operation principle discussed in Section 3, the voltage ripples across capacitors $C_{1,wind}$, $C_{2,wind}$, $C_{1,pv}$, $C_{2,pv}$ and C_o can be estimated as follows:

$$\Delta v_{c1,wind} = \frac{i_{D3,wind} D_{wind}}{C_{1,wind} f_s} \tag{24}$$

$$\Delta v_{c2,wind} = \frac{i_{D4,wind}(1 - D_{wind})}{C_{2,wind} f_s} \tag{25}$$

$$\Delta v_{c1,pv} = \frac{i_{D3,pv} D_{pv}}{C_{1,pv} f_s} \tag{26}$$

$$\Delta v_{c2,pv} = \frac{i_{D4,pv}(1 - D_{pv})}{C_{2,pv} f_s} \tag{27}$$

and

$$\Delta v_{co} = \frac{(i_{Lo} - I_o) D_{wind}}{C_o f_s} \tag{28}$$

From (24)–(28), the capacitances of $C_{1,wind}$, $C_{2,wind}$, $C_{1,pv}$, $C_{2,pv}$ and C_o can be readily computed.

5. Experimental Results

To verify the correctness of the theoretical analysis in this paper, a 1-kW prototype with the specifications summarized in Table 2 is built. The output inductor L_o is designed according to Section 4, which ensures CCM operation while output power is greater than 500 W. In Figure 7, the output power P_o is equal to 500 W. It can be seen that the inductor current i_{Lo} is twice the switching frequency and in BCM. This experimental measurement of i_{Lo} and inductor voltage v_{Lo} are identical to the conceptual waveforms depicted in Figure 6. Output power can be increased by enlarging the duty ratios of active switches. At 1-kW output, Figure 8 shows that the control signals $v_{sw,pv}$ and $v_{sw,wind}$ are still in an interleaved pattern but with larger duty ratio than that in Figure 7. In addition, the inductor current i_{Lo} is, indeed, in CCM. To examine the voltage and current stresses of the active switch, Figure 9 shows the practical voltage $v_{ds,wind}$ and current $i_{ds,wind}$ at full load, while $v_{ds,pv}$ and $i_{ds,pv}$ are shown in Figure 10. The $v_{ds,wind}$ and $i_{ds,wind}$ stand for the voltage and current of the active switches $SW_{1,wind}$ and $SW_{2,wind}$, as $v_{ds,pv}$ and $i_{ds,pv}$ do for $SW_{1,pv}$ and $SW_{2,pv}$. Figure 11 indicates that the output voltage can be kept at 400 V with the designed inductance, even if one of the renewable power sources shuts down. The DIPWC is able to accomplish a high conversion efficiency. Figure 12 depicts the measured efficiency from light load to full load, in which the peak efficiency is up to 95.4%. The practical measurement of the MPPT result at full load is shown in Figure 13. After MPPT, Figure 14 shows the steady-state output voltage of the PV module, v_{pv}, from which it can be seen that the output voltage fluctuates around a constant. In addition, Figure 15 is the picture of the DIPWC setup.

Table 2. The specifications of the DIPWC.

Symbols	Values & Types
v_{wind} (wind-turbine voltage)	120 V
v_{pv} (PV voltage)	80 V
V_{Co} (output voltage)	400 V
P_o (output power)	1 kW
f_s (switching frequency)	40 kHz
$L_{m,wind}$ (magnetizing inductance)	1.09 mH
$L_{m,pv}$ (magnetizing inductance)	1 mH
$L_{k,wind}$ (leakage inductance)	4.2 µH
$L_{k,pv}$ (leakage inductance)	4 µH
L_o (output inductance)	584 µH
n_{wind} (turns ratio of T_1)	2.12
n_{pv} (turns ratio of T_2)	2
$C_{1,wind}$ and $C_{2,wind}$ (capacitors)	47 µF
$C_{1,pv}$ and $C_{2,pv}$ (capacitors)	33 µF
C_o (output capacitor)	220 µF
$SW_{1,wind}$ and $SW_{2,wind}$ (switches)	IXFH120N20P
$SW_{1,pv}$ and $SW_{2,pv}$ (switches)	IXFH120N15P

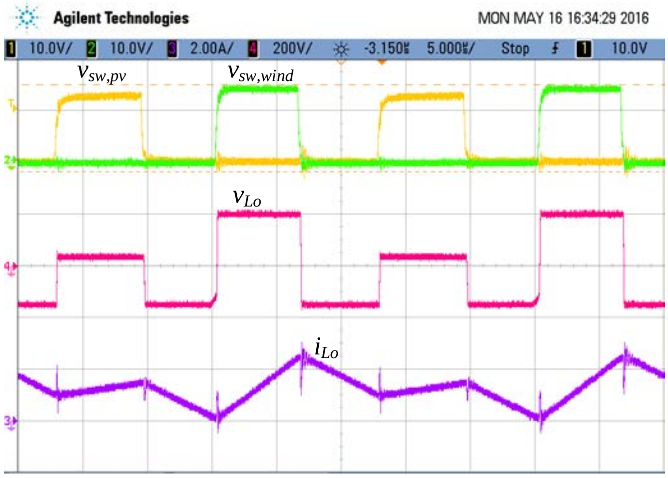

Figure 7. Measured waveforms while the output power is 500 W ($v_{sw,wind}$: 10 V/div, $v_{sw,pv}$: 10 V/div, v_{Lo}: 200 V/div, i_{Lo}: 2 A/div, time: 5 µs/div).

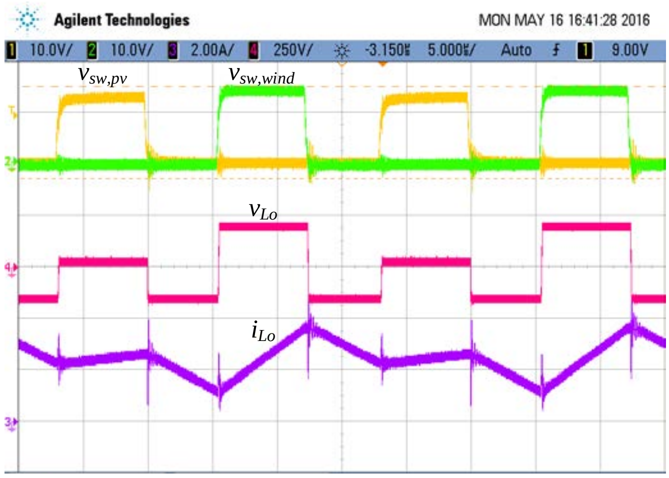

Figure 8. Measured waveforms while the DIPWC is operated at full load ($v_{sw,wind}$: 10 V/div, $v_{SW,pv}$: 10 V/div, v_{Lo}: 250 V/div, i_{Lo}: 2 A/div, time: 5 µs/div).

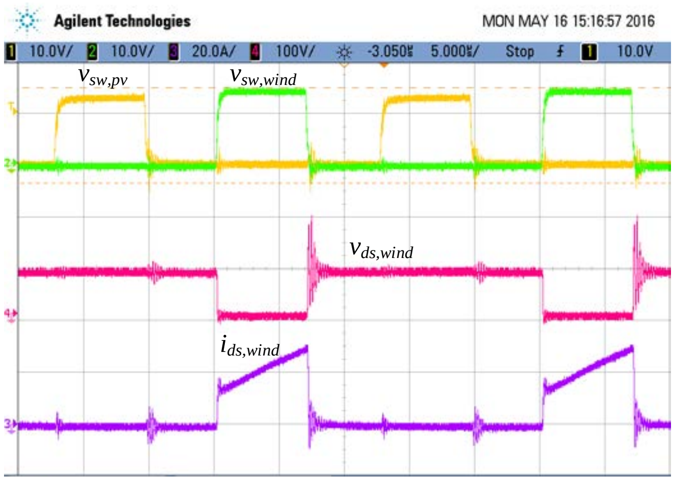

Figure 9. Measured waveforms of active switches at wind-turbine input port while the output power is 1 kW ($v_{sw,wind}$: 10 V/div, $v_{sw,pv}$: 10 V/div, $v_{ds,wind}$: 100 V/div, $i_{ds,wind}$: 20 A/div, time: 5 µs/div).

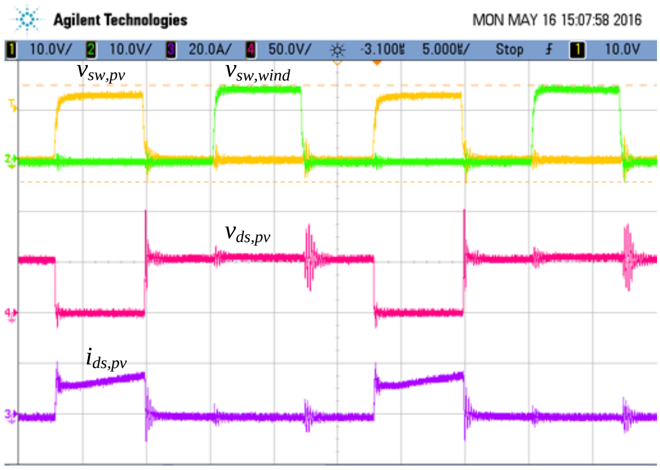

Figure 10. Measured waveforms of active switches at the PV input port while the output power is 1 kW ($v_{sw,wind}$: 10 V/div, $v_{sw,pv}$: 10 V/div, $v_{ds,pv}$: 50 V/div, $i_{ds,pv}$: 20 A/div, time: 5 µs/div).

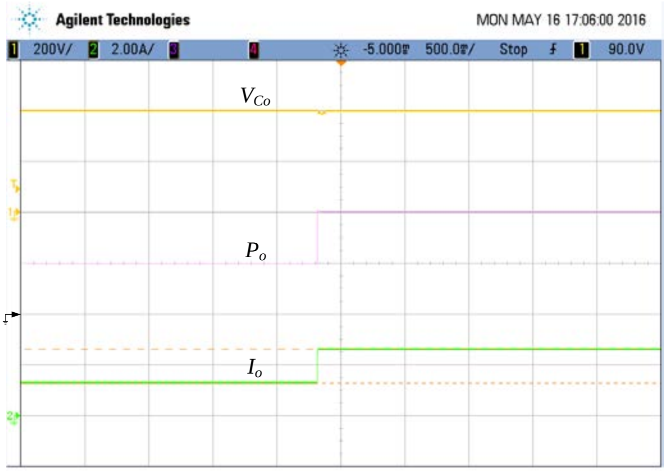

Figure 11. Measured waveforms to illustrate the transient response of the DIPWC ($v_{sw,wind}$: 10 V/div, $v_{sw,pv}$: 10 V/div, v_{Lo}: 200 V/div, i_{Lo}: 2 A/div, time: 5 µs/div).

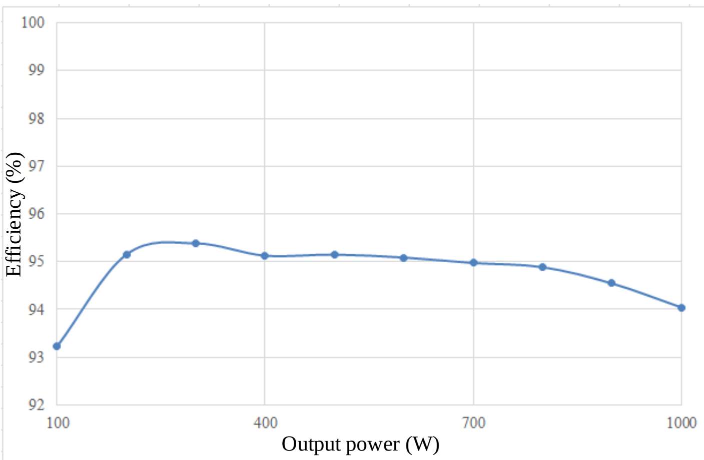

Figure 12. The measured efficiency from light load to full load.

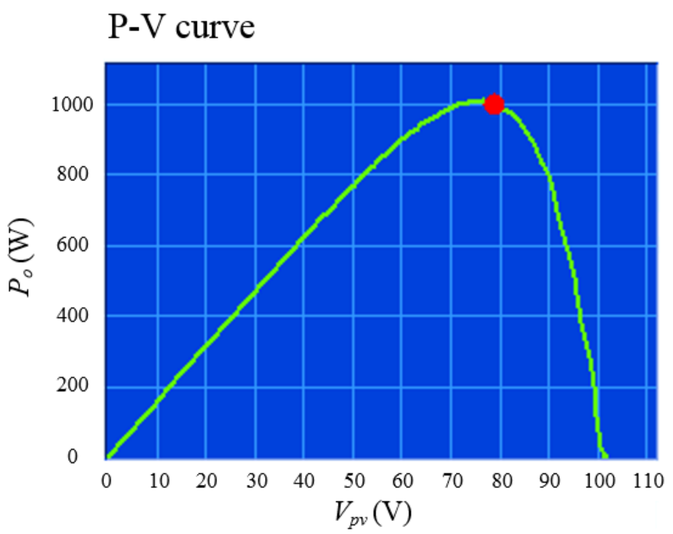

Figure 13. The practical MPPT result of the DIPWC at full load.

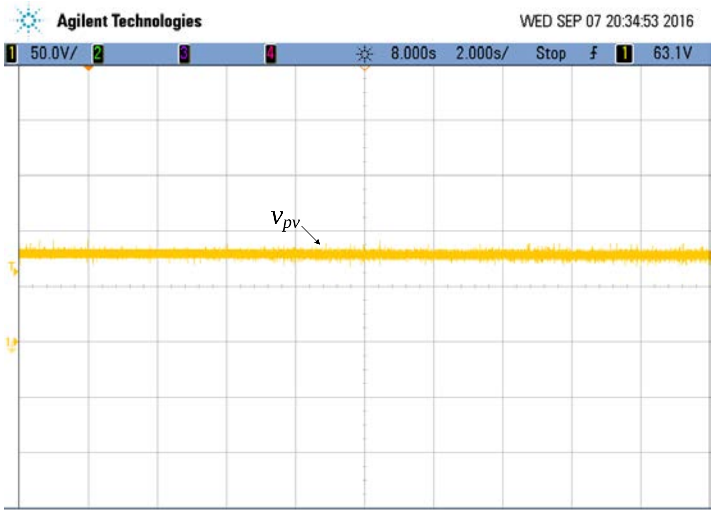

Figure 14. Output voltage of the PV module after MPPT and in steady state (v_{pv}: 50 V/div, time: 2 s/div).

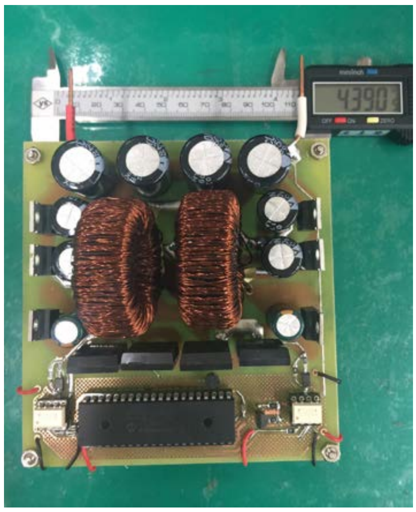

Figure 15. Picture of the DIPWC.

6. Conclusions

A novel DIPWC to process PV energy and wind-turbine power is first presented and then its operation principle is explored. The key power component in the DIPWC is the output inductor, which is designed with a detailed and theoretical derivation. To verify the correctness, a 1-kW prototype with the designed values is built and measured. Practical results validate the DIPWC. In addition, the feasibility and high-efficiency feature are also illustrated by the measurements.

Acknowledgments: The authors would like to convey their appreciation for grant support from the Ministry of Science and Technology (MOST) of Taiwan under its grant with reference number MOST 104-2221-E-327-036.

Author Contributions: Chih-Lung Shen and You-Sheng Shen conceived and designed the circuit. You-Sheng Shen performed simulations, carried out the prototype, and analyzed data with the guidance from Chih-Lung Shen. Chih-Lung Shen revised the manuscript for submission.

Conflicts of Interest: The authors declare no conflict of interest.

References

1. Alireza, K.; Mohamed, Y.A.R.I. Networked-based hybrid distributed power sharing and control for islanded microgrid systems. *IEEE Trans. Power Electron.* **2015**, *30*, 603–617.
2. Chunhua, P.; Peng, X.; Lei, P.; Rong, Y. Flexible robust optimization dispatch for hybrid wind/photovoltaic/hydro/thermal power system. *IEEE Trans. Smart Grid.* **2016**, *7*, 751–762.
3. Hussein, M.M.; Senjyu, T.; Orabi, M.; Wahab, M.A.A.; Hamada, M.M. Control of a stand-alone variable speed wind energy supply system. *Appl. Sci.* **2013**, *3*, 437–456. [CrossRef]
4. Yamada, H.; Kimura, K.; Hanamoto, T.; Ishiyama, T.; Sakaguchi, T.; Takahashi, T. A novel MPPT control method of thermoelectric power generation with single sensor. *Appl. Sci.* **2013**, *3*, 545–558. [CrossRef]
5. Lai, C.-M.; Yang, M.-J. A high-gain three-port power converter with fuel cell, battery sources and stacked output for hybrid electric vehicles and DC-microgrids. *Energies* **2016**, *9*, 180. [CrossRef]
6. Ramalu, T.; Mohd Radzi, M.A.; Mohd Zainuri, M.A.A.; Abdul Wahab, N.I.; Abdul Rahman, R.Z. A photovoltaic-based sepic converter with dual-fuzzy maximum power point tracking for optimal buck and boost operations. *Energies* **2016**, *9*, 604. [CrossRef]
7. Liu, F.; Wang, Z.; Mao, Y.; Ruan, X. Asymmetrical half-bridge double-input DC/DC converters adopting pulsating voltage source cells for low power applications. *IEEE Trans. Power Electron.* **2014**, *29*, 4741–4751. [CrossRef]
8. Sun, X.; Zhou, Y.; Wang, W.; Wang, B.; Zhang, Z. Alternative source-port-tolerant series-connected double-input DC–DC converter. *IEEE Trans. Power Electron.* **2015**, *30*, 2733–2742. [CrossRef]
9. Banaei, M.R.; Ardi, H.; Alizadeh, R.; Farakhor, A. Non-isolated multi-input–single-output DC/DC converter for photovoltaic power generation systems. *IET Trans. Power Electron.* **2014**, *7*, 2806–2816. [CrossRef]
10. Yang, P.; Chi, K.T.; Xu, J.; Zhou, G. Synthesis and analysis of double-input single-output DC/DC converters. *IEEE Trans. Ind. Electron.* **2015**, *62*, 6284–6295. [CrossRef]
11. Tsai, C.-T.; Shen, C.-L.; Su, J.-C. A power supply system with ZVS and current-doubler features for hybrid renewable energy conversion. *Energies* **2013**, *6*, 4859–4878. [CrossRef]
12. Piegari, L.; Rizzo, R.; Spina, I.; Tricoli, P. Optimized adaptive perturb and observe maximum power point tracking control for photovoltaic generation. *Energies* **2015**, *8*, 3418–3436. [CrossRef]
13. Park, S.; Park, Y.; Choi, S.; Choi, W.; Lee, K.-B. Soft-switched interleaved boost converters for high step-up and high-power applications. *IEEE Trans. Power Electron.* **2011**, *26*, 2906–2914. [CrossRef]
14. Hu, Y.; Deng, Y.; Long, J.; Lu, X. High step-up passive absorption circuit used in non-isolated high step-up converter. *IET Trans. Power Electron.* **2014**, *7*, 1945–1953. [CrossRef]
15. Li, W.; Xiang, X.; Li, C.; Li, W.; He, X. Interleaved high step-up ZVT converter with built-in transformer voltage doubler cell for distributed PV generation system. *IEEE Trans. Power Electron.* **2013**, *28*, 300–313. [CrossRef]
16. Liu, H.; Li, F.; Ai, J. A novel high step-up dual switches converter with coupled inductor and voltage multiplier cell for a renewable energy system. *IEEE Trans. Power Electron.* **2016**, *31*, 4974–4983. [CrossRef]
17. Liu, H.; Li, F. a novel high step-up converter with a quasi-active switched-inductor structure for renewable energy systems. *IEEE Trans. Power Electron.* **2016**, *31*, 5030–5039. [CrossRef]

18. Shen, C.-L.; Chiu, P.C. Buck-boost-flyback integrated converter with single switch to achieve high voltage gain for PV or fuel-cell applications. *IET Trans. Power Electron.* **2016**, *9*, 1228–1237. [CrossRef]
19. Tseng, S.-Y.; Wang, H.-Y. A photovoltaic power system using a high step-up converter for DC load applications. *Energies* **2013**, *6*, 1068–1100. [CrossRef]
20. Shen, C.-L.; Chen, H.-Y.; Chiu, P.-C. Integrated three-voltage-booster DC-DC converter to achieve high voltage gain with leakage-energy recycling for PV or fuel-cell power systems. *Energies* **2015**, *8*, 9843–9859. [CrossRef]
21. Lai, C.-M. Development of a novel bidirectional DC/DC converter topology with high voltage conversion ratio for electric vehicles and DC-microgrids. *Energies* **2016**, *9*, 410. [CrossRef]
22. Chen, Y.-M.; Liu, Y.-C.; Wu, F.-Y. Multi-input DC/DC converter based on the multiwinding transformer for renewable energy applications. *IEEE Trans. Ind. Appl.* **2002**, *38*, 1096–1104. [CrossRef]
23. Shi, X.; Jiang, J.; Guo, X. An efficiency-optimized isolated bidirectional DC-DC converter with extended power range for energy storage systems in microgrids. *Energies* **2013**, *6*, 27–44. [CrossRef]
24. Abramovitz, A.; Liao, C.-S.; Smedley, K. State-plane analysis of regenerative snubber for flyback converters. *IEEE Trans. Power Electron.* **2013**, *28*, 5323–5332. [CrossRef]